The role of midlatitude dry air during the withdrawal of the Indian summer monsoon

Deoras, A. ORCID: https://orcid.org/0009-0006-5407-6520, Turner, A. G. ORCID: https://orcid.org/0000-0002-0642-6876, Volonté, A. ORCID: https://orcid.org/0000-0003-0278-952X and Menon, A. ORCID: https://orcid.org/0000-0001-9347-0578 (2024) The role of midlatitude dry air during the withdrawal of the Indian summer monsoon. Quarterly Journal of the Royal Meteorological Society, 150 (765). pp. 5094-5112. ISSN 1477-870X doi: 10.1002/qj.4859 Available at https://centaur.reading.ac.uk/117866/

To link to this article DOI: http://dx.doi.org/10.1002/qj.4859

Publisher: Royal Meteorological Society

Received: 2 February 2024 | Revised: 15 May 2024 | Accepted: 6 August 2024

DOI: 10.1002/qj.4859

Quarterly Journal of the Royal Meteorological Society

RESEARCH ARTICLE

The role of midlatitude dry air during the withdrawal of the Indian summer monsoon

Akshay Deoras[1,2] | **Andrew G. Turner**[1,2] | **Ambrogio Volonté**[1,2] | **Arathy Menon**[3]

[1]National Centre for Atmospheric Science, University of Reading, Reading, UK

[2]Department of Meteorology, University of Reading, Reading, UK

[3]Met Office, Exeter, UK

Correspondence
Akshay Deoras, Department of Meteorology, University of Reading, Reading, RG6 6EG, UK.
Email: akshay.deoras@reading.ac.uk

Funding information
Weather and Climate Science for Service Partnership (WCSSP) India; Natural Environment Research Council, Grant/Award Number: NE/X000176/1

Abstract

The Indian summer monsoon supplies over 75% of the country's annual precipitation, profoundly impacting over a billion people. Variability in the timing of its onset and withdrawal has a direct impact on the agricultural sector and other users of water resources. Previous studies have shown that a wedge of mid-tropospheric dry air emanating from the midlatitudes is present over India during the pre-monsoon, which gradually retreats toward the northwest as the onset progresses. The withdrawal of the monsoon is observed to progress in a southeast direction during September–October, but there is a lack of a conceptual model. In this study, we use observations and the ERA5 reanalysis to understand the dynamics and thermodynamics of the withdrawal. We find that the climatological mid-level dry intrusion appears over northwest India around mid-September. Vertical profiles associated with this dry air show how the most unfavourable environment for deep convection occurs in the northwest, where the withdrawal occurs first. As the withdrawal progresses, the wedge of dry air deepens throughout its horizontal extent and descends, as well as pushing further across the country. This stabilises the troposphere, suppressing deep convection and ultimately driving the withdrawal toward the southeast. By mid-October, the dry air engulfs most of India, causing the monsoon to withdraw from the entire country. Thus, the strengthening of the mid-level dry advection from the midlatitudes can explain the withdrawal of the monsoon and its direction, in a reversal of the processes at work during progression of the onset. This work establishes a new paradigm for the withdrawal of the Indian summer monsoon in terms of midlatitude interactions, which could be tested for other monsoon regions.

KEYWORDS

deep convection, dry intrusion, Indian monsoon, surface fluxes, trajectories, withdrawal

1 | INTRODUCTION

The Indian summer monsoon (hereafter "the monsoon"), which lasts from June–September, is responsible for producing more than 75% of the annual precipitation in India (e.g., Parthasarathy & Mooley, 1978). It provides water that is important for summer crops, ground water recharge, hydroelectric power generation, industry, and basic human needs of over a billion people (Saha *et al.*, 1979; Preethi & Revadekar, 2013; Asoka *et al.*, 2018). The performance of the monsoon has a direct impact on the agriculture sector, which contributes to around 20% of India's gross domestic product (GDP; Zaveri *et al.*, 2016); a severe drought can reduce GDP by 2%–5%, whereas excess rainfall can increase GDP by up to 1.2% (Gadgil & Gadgil, 2006). Moreover, variability in the timing of the monsoon progression and withdrawal (i.e., the length of the rainy season) can affect the yield of summer crops (Prasanna, 2014; Amale *et al.*, 2023). For example, mature summer crops are damaged due to excessive rainfall during late September and October, which happens when there is a delay in the monsoon withdrawal. Accurate forecasting of the monsoon progression and withdrawal is therefore important, for which a proper understanding of the processes involved is essential.

The monsoon normally reaches Kerala, the southernmost state of India, around June 1 (Pai *et al.*, 2020). Its progression coincides with remarkable changes in the troposphere. Around the end of May, the large-scale meridional temperature gradient in the mid-to-upper troposphere (e.g., 600–200 hPa) between Eurasia and the Indian Ocean reverses (Xavier *et al.*, 2007). This indicates that the deep tropospheric heat source shifts northwards over the monsoon region, with the Tibetan Plateau acting as an elevated heat source (e.g., Flohn, 1957; Yanai *et al.*, 1992; Boos & Kuang, 2010). As a result, the subtropical westerly jet shifts north of the Tibetan Plateau, and the tropical easterly jet is established over India (e.g., Koteswaram, 1958). At lower levels, a cross-equatorial flow develops over the Indian Ocean in early summer. It strengthens in June, and a monsoon trough develops near the Himalayan foothills in the same month (e.g., Raju *et al.*, 2005). This supports the inflow of moisture from the Arabian Sea, as well as establishing southeasterly moisture flux into the Indo-Gangetic plain from the Bay of Bengal. The cross-equatorial flow is further intensified during June by increased moisture convergence and latent heat release (Mohanty *et al.*, 1984). Around mid-October, the meridional tropospheric temperature gradient reverts, shifting the deep tropospheric heat source southwards, indicating that the large-scale conditions supporting the monsoon circulation have collapsed (Xavier *et al.*, 2007). During this period, the subtropical westerly jet shifts southwards, there is an intrusion of dry continental air in response to a low-level anticyclone over northern and central India, the monsoon trough is displaced southward, and the low-level monsoon winds weaken (e.g., Rao, 1976).

One of the striking features of the monsoon is that the onset front propagates upwind relative to the northwesterly mid-level flow and perpendicular to the westerly or southwesterly low-level flow (Parker *et al.*, 2016). Thus, its progression cannot be explained simply in terms of the advection of moisture into India by low-level monsoon winds. Krishnamurti *et al.* (2012) used observed datasets and a high-resolution mesoscale model to understand the movement of onset isochrones between Kerala and New Delhi. They found that precipitation from anvils associated with deep convective clouds moistens the region ahead of isochrones, which makes the atmosphere conducive for convection. They also found that land-surface feedbacks are essential in the propagation of onset isochrones. Other modelling studies have also shown that land–atmosphere interactions play an important role in monsoon progression: Bollasina and Ming (2013) carried out simulations in a general circulation model by fixing the external forcing (i.e., solar insolation and sea-surface temperature) at monthly-mean values for May, and found that the monsoon still progressed over India. This suggests that land–atmosphere interactions and soil hydrology play a vital role.

Parker *et al.* (2016) used observations and the ERA-Interim reanalysis to understand the spatial progression of the monsoon. They found that the most favourable environment for deep convection and thus monsoon onset occurs in southern India first. Elsewhere in India, dry mid to low-level northwesterly air inhibits deep convection. However, detrainment from cumulus congestus clouds can moisten the dry air from below. As the advection of moisture from the Arabian Sea and subsequent moistening of the dry air strengthen, the monsoon propagates northwestwards (see their fig. 13 for a schematic of the conceptual model). The moistening of the dry air is reinforced by the land-surface wetting due to pre-onset rains, similar to the findings of Krishnamurti *et al.* (2012). The validity of the conceptual model presented in Parker *et al.* (2016) was confirmed by Volonté *et al.* (2020) and Menon *et al.* (2022) using high-resolution (~4 km) convection-permitting simulations of the Met Office Unified Model. Menon *et al.* (2022) found that wetting of the land surface due to pre-monsoon and onset rains moistens the boundary layer, which favours the initial progression of rainfall. However, mid-tropospheric moistening by advection plays the dominant role in further progression, since, following local onset, surface fluxes become less sensitive to variations in soil moisture.

Whilst the onset of the monsoon is marked by an abrupt reversal of winds over South Asia and a sharp increase in rainfall (e.g., Ananthakrishnan & Soman, 1988; Soman & Kumar, 1993), its withdrawal is more gradual (e.g., Bhat, 2006; Noska & Misra, 2016; Walker & Bordoni, 2016). Climatological dates published by the India Meteorological Department (IMD)[1] suggest the monsoon starts withdrawing from northwestern India by mid-September and is withdrawn from the entire country by mid-October. However, recent years have seen notable delays in the start of monsoon withdrawal, including the record delay of 2019 when the withdrawal commenced on October 9 and concluded within a week (i.e., on October 16: Sankar *et al.*, 2023). A contrasting situation was observed in 2013, when the withdrawal commenced on September 9 and concluded on October 21 (Arora *et al.*, 2014). This piques our interest in the mechanisms driving the progression of the withdrawal, which remain less understood compared with those driving the onset progression. This includes a lack of understanding of the interaction between moist convection and any return of the dry intrusion that is known to play an important role in monsoon progression (Parker *et al.*, 2016) and subseasonal breaks in the rain (e.g., Krishnamurti *et al.*, 2010).

The main aim of this study is to understand the dynamic and thermodynamic processes associated with the southeastward progression of the monsoon withdrawal. More specifically, this study explores the role of the interaction between the mid-level dry air emanating from the midlatitudes and moist convection in the monsoon withdrawal, for which we adapt the research framework of Parker *et al.* (2016) that was conceived for the onset. We present an outline of the data and methodology in Section 2, and explore climatological features of the withdrawal in Section 3. We then look at the kinematics of the withdrawal in Section 4, investigate the thermodynamics of the withdrawal in Section 5, and analyse surface fluxes in Section 6. We finally conclude in Section 7.

2 | METHODOLOGY AND DATA

2.1 | Selection of dates and locations for the analysis

We select September 15, September 30, and October 15 as the three climatological withdrawal dates for most analysis in this study. These dates represent the following key phases of the withdrawal process: September 15 (when the climatological withdrawal is about to begin), September 30 (mid-withdrawal), and October 15 (completion of the withdrawal). Figure 1 shows the location of climatological isochrones for these dates.[2]

Following Parker *et al.* (2016), we analyse profiles at Jodhpur (26.28°N, 73.02°E), Nagpur (21.08°N, 79.05°E), and Vizag (17.75°N, 83.25°E) in this study (see Figure 1 for their locations). These stations are aligned in parallel to the direction of the withdrawal and their locations in northwestern (Jodhpur), central (Nagpur), and southeastern (Vizag) India help us understand the contrast in airmass properties and the impact seen at the surface as the withdrawal of the monsoon evolves in a southeastward direction.

2.2 | ERA5 reanalysis

We use data from the European Centre for Medium-Range Weather Forecasts (ECMWF) ERA5 reanalysis (Hersbach

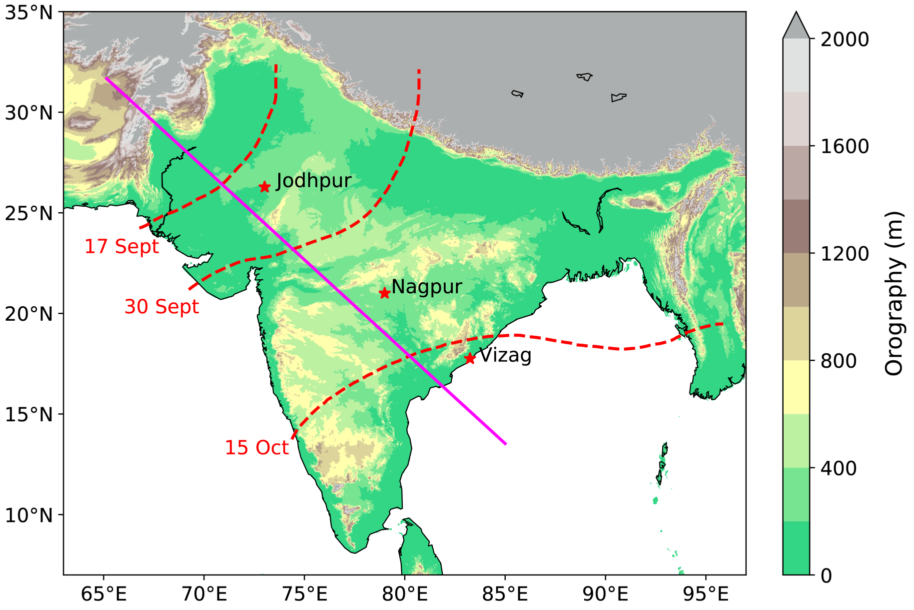

FIGURE 1 The orography (m) of South Asia along with locations of radiosonde stations (red stars) considered in the analysis. Dashed red lines show climatological isochrones of monsoon withdrawal as defined by the India Meteorological Department. A magenta line shows a transect used for computing vertical cross-sections of different fields in the analysis. The orography data are obtained from the National Center for Atmospheric Research TerrainBase dataset (National Geophysical Data Center, NESDIS, NOAA, US Department of Commerce, 1995). [Colour figure can be viewed at wileyonlinelibrary.com]

et al., 2020) to analyse composite dynamic and thermodynamic fields and to compute Lagrangian trajectories. ERA5 data are available globally on a 0.25° × 0.25° grid and at an hourly temporal resolution. These hourly data are used throughout the study other than for the trajectory analysis, for which six-hourly input data are used (see Section 2.7 for details). Of the 37 output pressure levels available, we consider those between 1000 and 200 hPa (both inclusive) with an interval of 50 hPa, although for the trajectory analysis all vertical levels available within that interval are used (every 25 hPa between 1000 and 750 hPa, every 50 hPa between 750 and 250 hPa, and every 25 hPa between 250 and 200 hPa).

The data used in this study cover withdrawal seasons from 1940 to 2022, allowing us to generate climatologies for 83 years. This has been made possible by the back-extension of the ERA5 final release data from 1959 to 1940, publicly available since March 2023 (Hersbach, 2023). The back-extension belongs to the pre-satellite era, when in situ observations were less widespread than today and there were no upper-air soundings before the mid-1940s. While the available data should be suitable for good synoptic-scale estimates in large parts of the Northern Hemisphere (Hersbach, 2023), the early 1940s see a reduced agreement in global mean surface temperature against reconstructions based only on observations and a cold low-stratosphere bias, potentially linked to the missing upper-air data. We therefore assessed the suitability of this back-extension by comparing the behaviour of the monsoon circulation and thermodynamic fields between 1940–1958 and 1959–2022. Having found no noticeable differences (see Sections 3,4, and 5.2), we decided to use the full time span of the ERA5 dataset, starting from 1940.

We also use the ERA5 dataset to analyse surface fluxes in Section 6. We note that the ERA5 dataset overestimates surface latent heat flux over land, including regions such as India (Martens *et al.*, 2020). However, the overestimation is reduced compared with its predecessor ERA-Interim, due to a better representation of land-surface processes in ERA5 (Martens *et al.*, 2020).

2.3 | APHRODITE rainfall

The rainfall dataset used in this study is the Asian Precipitation–Highly-Resolved Observational Data Integration Towards Evaluation (APHRODITE) gridded rain-gauge dataset for monsoon Asia (Yatagai *et al.*, 2012). It is available on a 0.5° × 0.5° grid, and consists of daily gauge inputs over 1951–2007. Prakash *et al.* (2015) compared the performance of six gridded rainfall datasets (GPCP, CMAP, CPC, APHRODITE, CRU, and GPCC) with that of the IMD's own gridded rainfall dataset for 27 monsoon seasons (1979–2005). They found that the performance of APHRODITE was better than that of most other products considered.

2.4 | MERGIR infrared brightness temperature

We use the global merged infrared (MERGIR) brightness temperature dataset produced by the Climate Prediction Center and National Centers for Environmental Prediction (Janowiak *et al.*, 2001) to examine the frequency of occurrence of deep convection. The dataset contains 4-km pixel-resolution data of infrared brightness temperature (IRBT) from 2000 onwards at a temporal resolution of 30 minutes for the 60°S–60°N domain. The IRBT product merges data from geostationary satellites launched by the United States, Europe, and Japan. If the minimum IRBT at a grid point on a given day does not exceed 233.15 K (−40 °C), we declare the occurrence of deep convection at that grid point. This IRBT threshold of 233.15 K is widely adopted for detecting the presence of deep convective clouds (e.g., Taylor *et al.*, 2017).

2.5 | Upper-air data

To provide more detailed vertical profiles at individual locations and for an in situ comparison of the gridded reanalysis data, we obtain radiosonde data from the Integrated Global Radiosonde Archive (IGRA) and compute mean profiles for the period 1971–2019. We analyse the radiosonde data for Jodhpur (station ID: 42339), Nagpur (station ID: 42867), and Vizag (station ID: 43150), using launches at 1200 UTC for pentads centred on September 15, September 30, and October 15. Parker *et al.* (2016) had combined the data from radiosonde launches at 0000 UTC and 1200 UTC for their analysis (see their fig. 6). However, we consider data from radiosonde launches at 1200 UTC only, for two reasons. Firstly, as noted by Parker *et al.* (2016), the frequency of radiosonde launches at 0000 UTC is larger than that at 1200 UTC in the IGRA dataset. The mean profile at a location will therefore be skewed, which is illustrated by the presence of a nocturnal stable layer near the surface at Jodhpur and Nagpur (see their fig. 6). Secondly, analysing profiles at 1200 UTC instead of 0000 UTC will help us understand the atmospheric instability better during the local afternoon hours, when convective storms typically form. For each station, the data are first linearly interpolated between the surface level (where available) and 100 hPa in order to have each sounding on a consistent set of pressure levels. Profiles are then averaged to get a composite mean for each station.

2.6 | ISCCP dataset

We use the International Satellite Cloud Climatology Project (ISCCP) H-series dataset (Rossow *et al.*, 2022; Young *et al.*, 2018) to estimate the height of clouds at different locations before and after the withdrawal. The H-series dataset is developed using input data from full-resolution Advanced Very High Resolution Radiometer Global Area Coverage and images from polar as well as geostationary satellites, covering the period July 1983–June 2017. It is available at a temporal resolution of three hours and a spatial resolution of 1° × 1°. We use the cloud-top pressure field, which represents the location of the radiating top of clouds. This field is obtained from cloud-top temperature.

2.7 | Lagrangian trajectories

Lagrangian trajectories are a powerful tool for airmass analysis, as they can identify their origin and the processes occurring as air parcels travel along them. In this study, we use them to illustrate changes in the flow direction and properties such as pressure and specific humidity of low and mid-level air flowing over northern India during withdrawal of the monsoon.

We compute Lagrangian trajectories using the Lagrangian analysis tool LAGRANTO (Sprenger & Wernli, 2015), building on techniques recently applied to both tropical and midlatitude weather systems (see Volonté *et al.*, 2020, 2022 for recent application to the progression of the Indian and East Asian summer monsoons). LAGRANTO uses a three-time iterative forward Euler scheme with an iteration step equal to 1/12 of the time spacing of the input data (i.e., 30 minutes for the six-hourly ERA5 data used in this work). As specified in Section 2.2, ERA5 is available at an hourly temporal resolution, as used elsewhere in this study. However, our choice to use the six-hourly input data is justified not only by storage constraints (i.e., the need to use all available vertical levels in the troposphere) but also by previous literature. The climatological properties of the airmasses involved in the progression of the East Asian summer monsoon are illustrated with clarity by trajectories calculated from the six-hourly input data in Volonté *et al.* (2022). Trajectories using six-hourly and three-hourly input data were used successfully to depict the monsoon progression in a single season by Volonté *et al.* (2020). Three-hourly ERA5 input data were also used successfully in Rai and Raveh-Rubin (2023), where Lagrangian trajectories are the key methodology in the analysis of cross-equatorial dry intrusions. Turning our attention beyond Asia, Madonna *et al.* (2014) were able to use six-hourly ERA-Interim reanalysis data to produce a global climatology of warm conveyor belts that is still used as a point of reference in the field. These works show that using three- to six-hourly input data is appropriate for climatological trajectories of synoptic or larger-scale phenomena, the typical life-cycles of which are closer to 1–2 days rather than just a few hours. Therefore, the six-fold increase in computing time associated with using the native hourly frequency of ERA5 data would not be justified by a gain in trajectory accuracy.

Backward trajectories are computed by using the instantaneous three-dimensional wind field to calculate prior positions of the selected air parcels. For each year, 50 trajectories (25 starting at 600 hPa and 25 at 850 hPa) are released at 0000 UTC on September 15, September 30, and October 15, and are computed backward for six days. Following Parker *et al.* (2016), trajectories are released from a small region over northern India (27°–28°N, 77°–78°E, with a release horizontal spacing of 0.25°). Trajectories are stopped when leaving the horizontal domain of the input data (35°S–75°N, 15°E–145°E) or when exceeding its upper boundary (200 hPa), and they re-enter the atmosphere when hitting the ground. Local values of relevant physical quantities, such as pressure and specific humidity, are interpolated onto the trajectories to assess their variations along the flow.

3 | LARGE-SCALE CLIMATOLOGICAL FEATURES OF THE WITHDRAWAL

In this section, we investigate the large-scale features of the withdrawal. We first characterise the withdrawal using pentad-mean precipitation and then analyse the occurrence of deep convection using IRBT centred on September 1,[3] September 15, September 30, and October 15 and averaged over 1951–2007 and 2000–2022, respectively. These analyses will help us understand changes in precipitation, intensity of convection, and the large-scale circulation relative to the monsoon withdrawal.

Figure 2b–d shows the relationship between precipitation and climatological withdrawal isochrones considered by the IMD (Pai *et al.*, 2020). The pre-withdrawal scenario centred on September 1 is also shown (Figure 2a). On September 1, the most intense precipitation ($\geq$12 mm·day^{-1}) occurs over central, western, and northeastern India. Over northwestern India, from where the monsoon withdrawal commences, the magnitude of precipitation is already small ($\leq$2 mm·day^{-1}). As the withdrawal isochrone moves southeastwards from

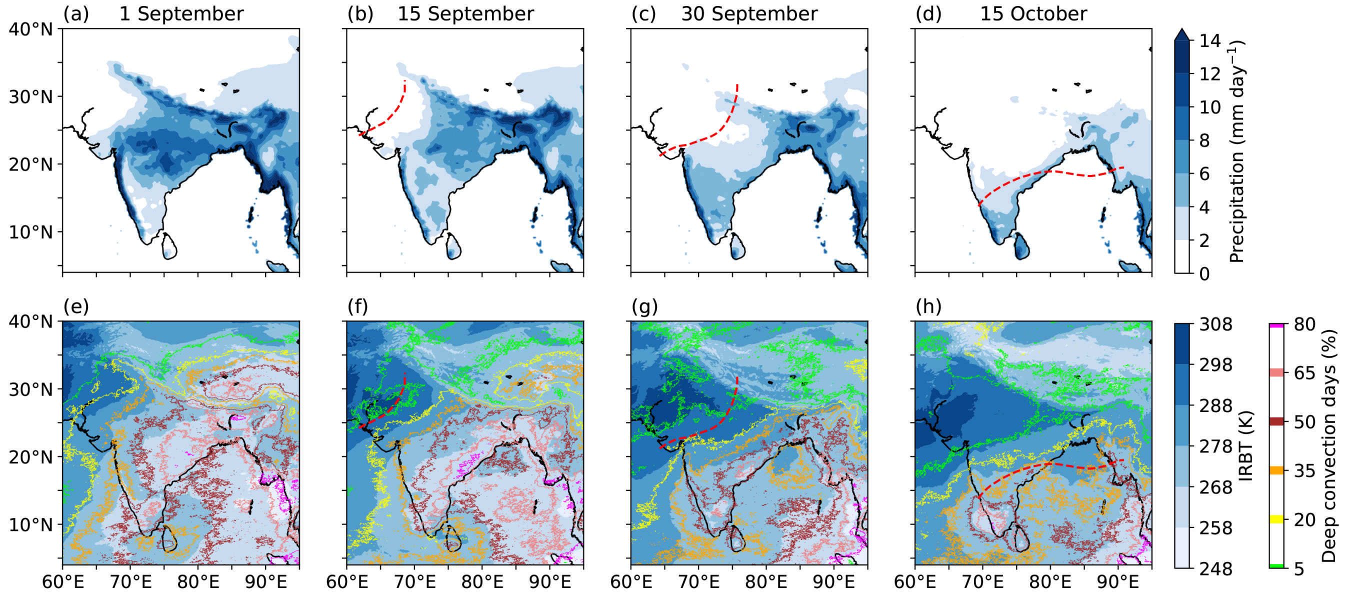

FIGURE 2 (a–d) Pentad mean precipitation (mm·day^{-1}) averaged over 1951–2007 (top panel), and (e–h) pentad mean infrared brightness temperature (IRBT; K) averaged over 2000–2022 (bottom panel). Coloured line contours in (e)–(h) show the percentage of days with deep convection (IRBT≤233.15 K) at each grid point in the respective pentads during 2000–2022. Each pentad is centred on the dates shown in the top panel. Dashed red lines show climatological isochrones of the monsoon withdrawal as defined by the India Meteorological Department. The isochrones are shown for (b,f) September 17, (c,g) September 30, and (d,h) October 15. Note that the isochrone for September 15 is not shown, since the withdrawal initiates on September 17. [Colour figure can be viewed at wileyonlinelibrary.com]

mid-September to mid-October, there is a sharp reduction in precipitation behind it (Figure 2b–d). Whilst light precipitation (2–4 mm·day^{-1}) can still occur in areas where the isochrone is located (e.g., parts of the Himalayan foothills on September 30), precipitation is always most intense to its south. Interestingly, northeast India (i.e., states such as Mizoram) continues to receive light precipitation on October 15 despite the monsoon withdrawal.

Figure 2e–h shows pentad-mean composites of IRBT and the frequency of occurrence of deep convection (coloured line contours; defined when IRBT≤ 233.15 K, see Section 2.4) in respective pentads from 2000 to 2022. Prior to the monsoon withdrawal, deep convection over northwestern India occurs on approximately 35% of days in the analysis period (Figure 2e). However, this decreases to approximately 5% as the monsoon withdraws around the end of September (Figure 2f) and to almost 0% by mid-October (Figure 2h). Deep convection is most frequent over the southeastern coast of India when the withdrawal commences from northwestern India (Figure 2f). The subsequent reduced occurrence of deep convection (Figure 2f–h) suggests that deep convection retreats southeastwards during the withdrawal, consistent with the reduction in precipitation amount (Figure 2b–d). In fact, this retreat of deep convection is the reverse of the conceptual model proposed by Parker *et al.* (2016) for progression of the monsoon onset. This result suggests the potential role of a dry intrusion from the northwest in inhibiting deep convection.

We now examine relative humidity and winds (Figure 3) in order to check for the presence of a dry intrusion during monsoon withdrawal. We analyse the same range of pressure levels (i.e., 925, 850, 750, and 600 hPa) as Parker *et al.* (2016), who determined that the 600-hPa level in particular is located at the heart of dry intrusions. At 600 hPa on September 15 (Figure 3a), there is a reservoir of dry air over Pakistan, Afghanistan, and northern parts of the Arabian Sea. Many previous studies have reported the presence of this reservoir during the mature monsoon of July and August (e.g., Krishnamurti *et al.*, 2010; Singh & Sandeep, 2022); a deep intrusion of this dry air into India can lead to breaks in the monsoon rains (e.g., Bhat, 2006; Krishnamurti *et al.*, 2010; Singh & Sandeep, 2022).

The composite shown in Figure 3a reveals an intrusion of dry northwesterly winds into Rajasthan. Whilst there are weak northwesterly winds over this region at 750 hPa (Figure 3d), the air is more humid than at 600 hPa. At lower levels (Figure 3g,j), the air is considerably more humid due to the advection of moisture from the Arabian Sea by the Somali jet. The monsoon trough can be seen over eastern India at these levels. On September 30, the dry intrusion over northwestern India at 600 hPa strengthens (Figure 3b), and the air in lower levels starts

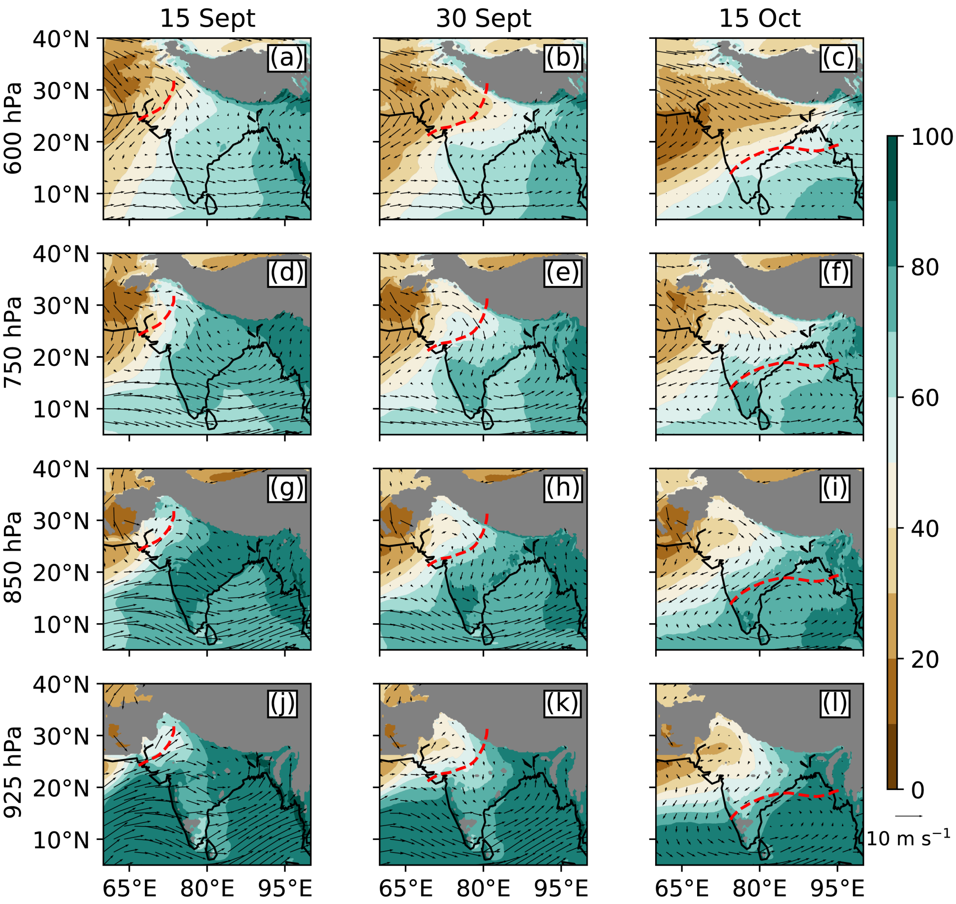

FIGURE 3 Pentad mean relative humidity (shading; %) and winds (vectors; m·s^{-1}) centred on (a,d,g,j: left) September 15, (b,e,h,k: middle) September 30, and (c,f,i,l: right) October 15, over the years 1940–2022. Dashed red lines show climatological isochrones of monsoon withdrawal as defined by the India Meteorological Department. The isochrones are shown for (left) September 17, (middle) September 30, and (right) October 15. Grey areas in each subplot indicate where the mean surface pressure is less than the pressure level shown in the subplot. Note that the isochrone for September 15 is not shown, since the withdrawal initiates on September 17. [Colour figure can be viewed at wileyonlinelibrary.com]

becoming dry (relative humidity≤50%; Figure 3e,h,k). The monsoon trough shifts southwards over the east coast of India (Figure 3h), causing weakened winds over the Bay of Bengal. At all levels, the air behind the withdrawal isochrone is much drier than that ahead of it. At 925 hPa (Figure 3k), the penetration of monsoon winds from the Arabian Sea starts weakening. On October 15, the dry intrusion at 600 hPa (Figure 3c) has expanded into central India and there is a sharp gradient in relative humidity at this level behind and ahead of the withdrawal isochrone. Figure 3f,i,l shows conditions at lower levels. The monsoon trough, which is indicated by a convergent region over eastern India at 850 hPa (Figure 3i), shifts to peninsular India, and there is no longer the penetration of monsoon winds from the Arabian Sea into India. Only the winter monsoon winds (i.e., the northeast monsoon) are active over the peninsula. Over northeastern India, low-level convergence, which supplies moisture from the Bay of Bengal, could be causing precipitation after the monsoon withdrawal (Figure 2d). In order to assess the quality of the ERA5 dataset during the back-extension period, we analyse composites of lower and mid-tropospheric relative humidity and winds for 1940–1958 and 1959–2022 (Figures S1 and S2). There are no noticeable differences between the two composites, suggesting the suitability of using the ERA5 dataset for the period 1940–2022.

In summary, light precipitation is observed over northwestern India during early September, which is two weeks prior to the monsoon withdrawal. Whilst deep convection can occur here, it is most frequent over the southeast coast. In early September, many parts of India still receive substantial precipitation. Around mid-September, a dry intrusion from the northwest at 600 hPa first suppresses deep convection over northwestern India, forcing the monsoon to start withdrawing from there. The subsequent intrusion of the dry air into India regulates the monsoon withdrawal in the southeast direction during late September and October. This appears to be the reverse of the conceptual model proposed by Parker *et al.* (2016), to be investigated further.

4 | KINEMATICS OF THE WITHDRAWAL

In this section, we compute Lagrangian back trajectories in order to provide a complete description of the origin, path, evolution and any interaction between the airmasses involved in the monsoon withdrawal. The maps in the top two rows of Figure 4 illustrate how the mid- and low-level

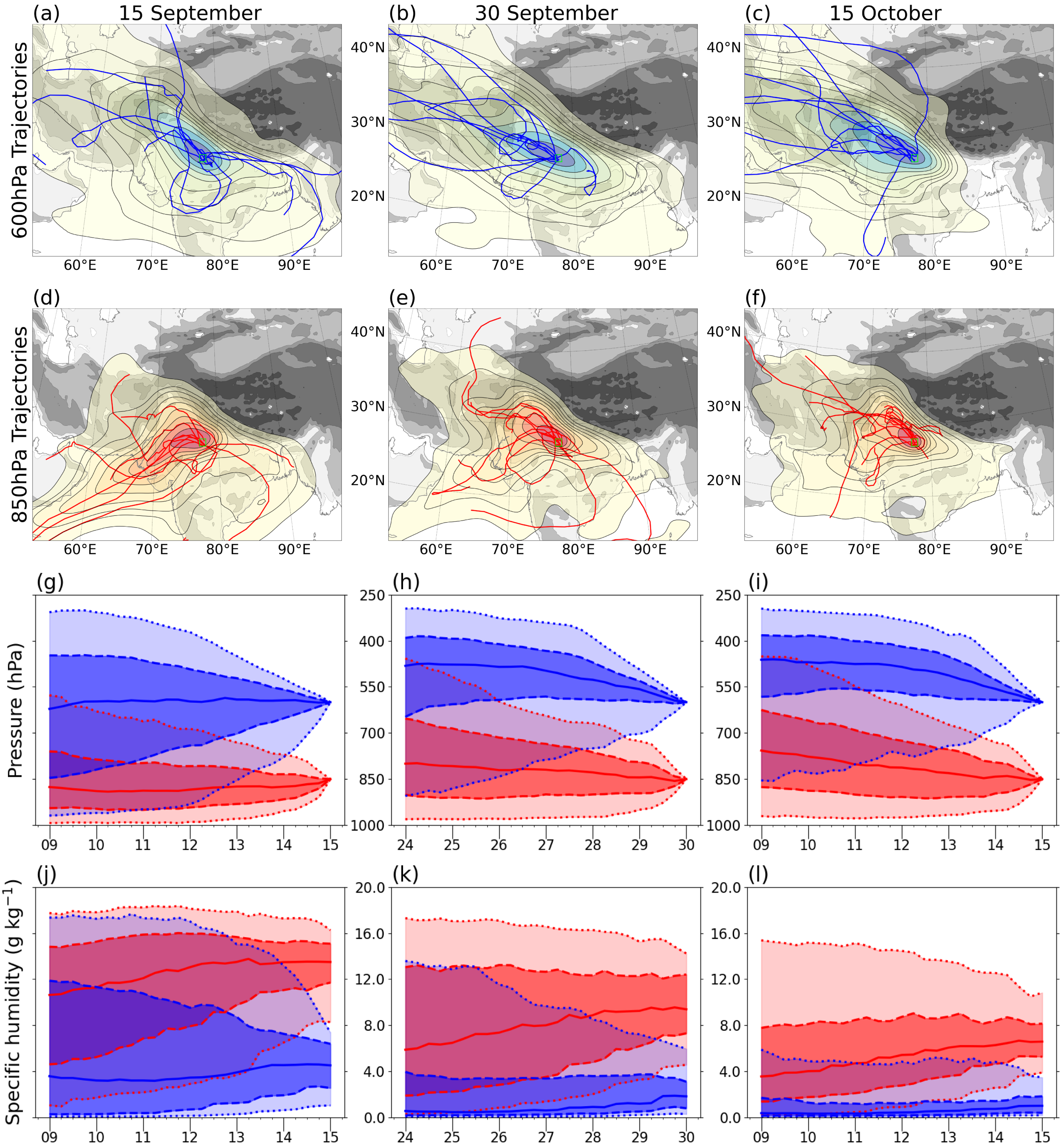

FIGURE 4 (a–f) Six-day backward trajectories released at (a–c) 600 hPa and (d–f) 850 hPa from the small green box at 0000 UTC on the dates shown in the title for all years from 1940 to 2022 (see Section 2.7 for details on the trajectory calculation). The kernel density estimate of trajectory points (a–f) is shown for each case (shading, with intervals every 10% of the maximum density). The 10 individual trajectories shown in each of the panels (blue and red lines) are chosen by sorting all trajectories by the angle between their origin point and the centre of the release region and then selecting the central trajectory of each decile. Time evolution of (g–i) pressure (hPa) and (j–l) specific humidity (g·kg^{-1}) along trajectories shown in blue for trajectories starting at 600 hPa and in red for those starting at 850 hPa. Solid lines in (g–l) show the median of each field, dashed lines with dark shading between them show the 25th and 75th percentiles, and dotted lines with light shading between them show the 5th and 95th percentiles. Percentiles are calculated independently at each time, hence a single percentile line can refer to different trajectories at different times. [Colour figure can be viewed at wileyonlinelibrary.com]

flow arriving over northern India (exemplified by back trajectories released at 600 and 850 hPa, respectively) evolves during this period, captured by three trajectory release dates (September 15, September 30, and October 15).

In particular, Figure 4a–c shows the trajectory density extending northwestward, indicating that the remote northwest gradually becomes the predominant origin for the mid-level flow. As indicated by the "decile" trajectories (see figure caption for more details), around 60% of the trajectories arriving on September 15 originate from the northwestern quadrant, increasing gradually to exceed 80% by October 15. Time-evolving pressure fields in Figure 4g–i for the full sets of trajectories show that the spread in pressure decreases as the mid-level flow evolves towards northwesterly (blue lines and shading). Trajectories within the interquartile range of the September 15 subset extend down to pressure values of almost 850 hPa at their origin, while they are confined to pressures close to or lower than 600 hPa in the later subsets. This indicates that the northwesterly airmass becomes more coherent and limited to air of mid and upper tropospheric origin as the seasonal cycle evolves. At the same time, Figure 4j–l shows a decrease in specific humidity as the season progresses. The median value is close to 4 $\mathrm{g\cdot kg^{-1}}$ throughout the lifetime of the September 15 trajectories, but nearly zero in later trajectories. The 75th percentile of specific humidity also reduces substantially, with origin values decreasing from 16 $\mathrm{g\cdot kg^{-1}}$ to 4 $\mathrm{g\cdot kg^{-1}}$ and then 2 $\mathrm{g\cdot kg^{-1}}$ through the three withdrawal stages. These results indicate a decline in the proportion of trajectories that had ascended to the mid-troposphere from lower altitudes; instead, the mid-level flow becomes composed almost exclusively of dry northwesterlies flowing in the mid and upper troposphere.

Focusing on the flow arriving at the low-level trajectory target region, Figure 4d–f shows that in the initial withdrawal stage its main origin is westerly flow from over the Arabian Sea, typical of the monsoon season. However, around 20% of the trajectories reach the target region from the east, with a "decile" trajectory indicating clear cyclonic flow over eastern India and the Bay of Bengal, which points to the role of the monsoon trough in the circulation in the area. A third airmass origin, from the northwest, becomes important (roughly 30% of cases) by September 30, with "decile" trajectories flowing around the Hindukush mountain range in their journey towards northern India. As cyclonically recurving trajectories and those flowing over the Arabian Sea gradually decrease in number, the westerly origin dominates by October 15, although at a short distance from the target box. Looking at the time evolution of pressure and specific humidity (Figure 4g–i and j–l, respectively), we can see that the interquartile pressure spread of the low-level flow at its origin is larger in late-stage trajectories, as both the median and 75th percentile of pressure at the origin decrease (i.e., their height increases) as the season progresses. At the same time, the fraction of descending trajectories (those increasing pressure with time) becomes larger. Specific humidity decreases as the seasonal cycle evolves, with the values at the median origin going from around 11 $\mathrm{g\cdot kg^{-1}}$ to just above 3 $\mathrm{g\cdot kg^{-1}}$, although the general pattern of moisture increase along the trajectory (of 2–3 $\mathrm{g\cdot kg^{-1}}$) is maintained. These results highlight the transition from a flow mostly confined to low altitudes (part of the Somali Jet or flowing around the monsoon trough) towards a situation in which descending air of mid-level origin contributes a larger portion of the low-level flow arriving over the target region. In order to assess the quality of the ERA5 dataset during the back-extension period, we analyse maps of low and mid-level trajectories for 1940–1958 and 1959–2022 (Figures S3 and S4). No fundamental differences can be found between the two composites, suggesting the suitability of using the ERA5 dataset for the period 1940–2022.

To summarise, during the withdrawal of the monsoon we see the increasing importance of dry mid and upper tropospheric airmasses originating from the northwest before arriving over northern India. This is particularly evident in the mid-level flow, but it can also be seen at lower altitudes. At the same time, we see that moist airmasses flowing at low altitudes over the Arabian Sea increasingly struggle to reach our target region over northern India, gradually being replaced by descending northwesterly dry air.

5 | THERMODYNAMICS OF THE WITHDRAWAL

Here we analyse upper-air observations and investigate vertical cross-sections of thermodynamic fields in order to help understand how changes in atmospheric thermodynamics control the progress and direction of the monsoon withdrawal.

5.1 | Analysis of radiosonde data

Figure 5 shows tephigrams for Jodhpur, Nagpur, and Vizag. We select these locations broadly since they are aligned in parallel to the direction of withdrawal (see Section 2.1 and Figure 1). We first analyse profiles for Jodhpur, since the withdrawal progresses from there toward the southeast (i.e., Vizag).

Small convective available potential energy (CAPE; the positive area on the tephigram where the parcel is warmer than the environment) can be seen at Jodhpur prior to the local climatological withdrawal on September 17

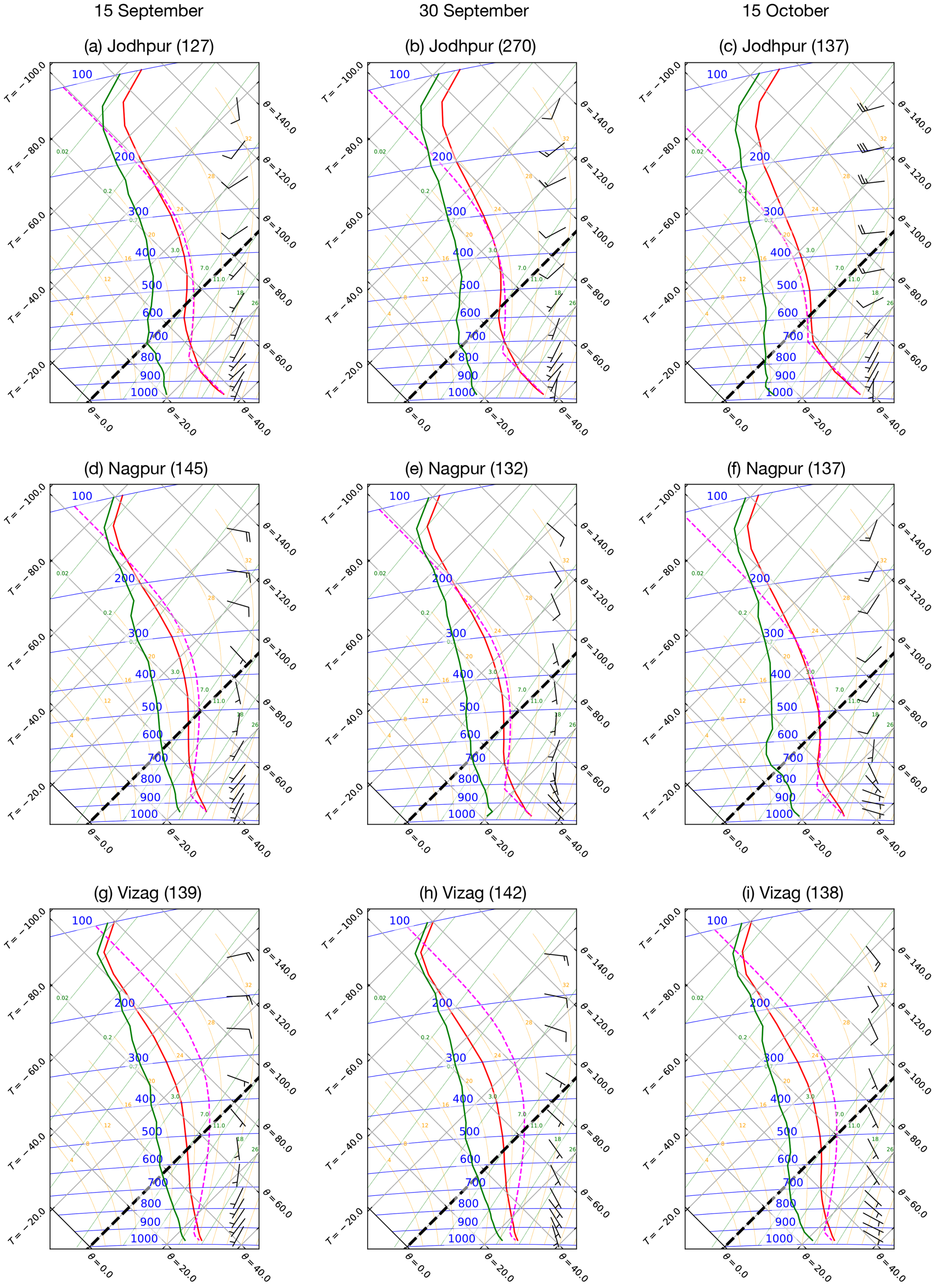

FIGURE 5 Tephigrams showing climatological mean radiosonde profiles from (a–c) Jodhpur, (d–f) Nagpur, and (g–i) Vizag during 1971–2019. Temperature (solid red), dewpoint (solid green), and parcel (dashed magenta) profiles at 1200 UTC are plotted for pentads centred on (a,d,g) September 15 (left), (b,e,h) September 30 (middle), and (c,f,i) October 15 (right). Numbers in brackets in the title show the number of radiosonde launches. Thick dashed black lines represent the freezing level. Tilted solid green lines show the saturation mixing ratio ($g \cdot kg^{-1}$), solid blue lines show isobars (hPa), tilted solid grey lines show isotherms (°C) and dry adiabats (°C), and solid orange lines show moist adiabats (°C). Note that observations at 975 hPa are not available in (d), and wind barbs are not shown at all vertical levels in order to reduce the clutter in the figure. [Colour figure can be viewed at wileyonlinelibrary.com]

(Figure 5a). However, a reduction in CAPE suggests that the convective instability decreases following the monsoon withdrawal (Figure 5b). In fact, the profile attains absolute stability on October 15 (Figure 5c). Between September 15 and October 15, the dewpoint depression in mid and low levels increases, and the lifted condensation level (LCL) rises from approximately 800 hPa to approximately 700 hPa. At upper levels (e.g., 200 hPa), there are southwesterly winds on September 15, which become westerly and intensify by October 15, indicating southward migration of the subtropical jet stream. There is a small increase in the low-level temperature between September 15 and September 30.

The tephigrams for Nagpur in central India (Figure 5d–f) feature a similar pattern of increasing dewpoint depression at mid and low levels (especially between 700 and 600 hPa) and increasing stability. The tropical easterly jet weakens and upper-level winds become southwesterly on October 15, whereas southwesterly winds at low levels become southeasterly.

Unlike for Jodhpur and Nagpur, convection over Vizag persists between September 15 and October 15 (Figure 5g–i) due to the winter monsoon. In fact, the reduction in CAPE in this period is much smaller than at Jodhpur and Nagpur. Furthermore, there is only a small impact of the mid-level dry intrusion at Vizag, agreeing with Figure 3. At low levels, the wind direction shifts from southwesterly to southeasterly, indicating the onset of the winter monsoon.

Parker *et al.* (2016) found that low levels (especially between 800 and 600 hPa) at the three locations evolve from a dry adiabatic profile to a pseudoadiabatic profile as the monsoon progresses (see their fig. 6). On September 15, the profile between the surface and ~800-hPa level at Jodhpur is already dry adiabatic (Figure 5a), and as the withdrawal progresses, the profile between the surface and ~700 hPa becomes dry adiabatic by October 15 (Figure 5c). At Nagpur, profiles evolve in a similar pattern between September 15 and October 15 (Figure 5d–f). In contrast, profiles at Vizag remain nearly pseudoadiabatic through this period, suggesting a weaker impact of dry air than at Jodhpur and Nagpur. At all times and locations, the profile at higher levels (above ~600 hPa) is nearly pseudoadiabatic, which is commonly observed in the Tropics (e.g., Betts, 1986).

5.2 | Vertical cross-sections of thermodynamic reanalysis fields along a transect

Following Parker *et al.* (2016), we now analyse vertical cross-sections of thermodynamic fields along a northwest-to-southeast transect shown in Figure 1. This will help us analyse the thermodynamic structure in more spatial detail by considering additional locations along the direction of the withdrawal instead of just the three locations considered for radiosonde analysis (Section 5.1).

The vertical cross-sections are computed for September 15 (Figure 6a,d,g,f), September 30 (Figure 6b,e,h,k), and October 15 (Figure 6c,f,i,l) over 1940–2022. Figure 6a shows a wedge of air with high water-vapour mixing ratio at low levels that deepens to the southeast. As the monsoon withdrawal continues, the relatively dry mid-level flow from the northwest strengthens and the depth of the low-level westerly mean flow decreases (Figure 3). As a result, the moist low-level air along the transect becomes drier as the withdrawal progresses (Figure 6a–c). Over the Bay of Bengal, the water-vapour mixing ratio remains fairly constant and its vertical gradient is more uniform than over northwest India. The height of the LCL over India increases between September 15 and October 15 (Figure 6a–c).

Vertical cross-sections of relative humidity (Figure 6d–f) show the retreat of moist air over India as the dry intrusion from the northwest penetrates and descends into India. Given that relative humidity exerts significant control on the occurrence of deep convection, we see a decline in the occurrence of deep convection over central India on September 30 (Figure 2g), and hypothesise that even cumulus clouds would be of limited vertical extent. The deepening of the dry layer over this region on October 15 limits the occurrence of deep convection further, which can be seen in Figure 2h. Deep convection is favoured over the southeast coast of India at this time (also seen in Figure 2h).

To look in more detail at the dry intrusion, we analyse vertical cross-sections of equivalent potential temperature (θ_e) along the transect (Figure 6g–i). The intrusion of low-θ_e air from the northwest stands out on September 15 (Figure 6g), and θ_e is smallest just below the freezing level (at approximately 600 hPa). As the withdrawal progresses, the high-θ_e air at low levels over India is replaced by low-θ_e air. By October 15 (Figure 6i), the high-θ_e air is confined to the southeast coast of India and adjoining parts of the Bay of Bengal, consistent with the start of the winter monsoon there.

We now analyse saturated equivalent potential temperature (θ_es), since it is useful in identifying moist convective regimes. A constant θ_es with height indicates a near-pseudoadiabatic profile. θ_es at the 600–200-hPa level remains fairly constant along the transect at all times. Jodhpur, Nagpur, and Vizag are located near the transect (Figure 1), and tephigrams for these sites exhibit a near-pseudoadiabatic profile over the 600–200-hPa levels (Figure 5). On September 15, there is a strong vertical

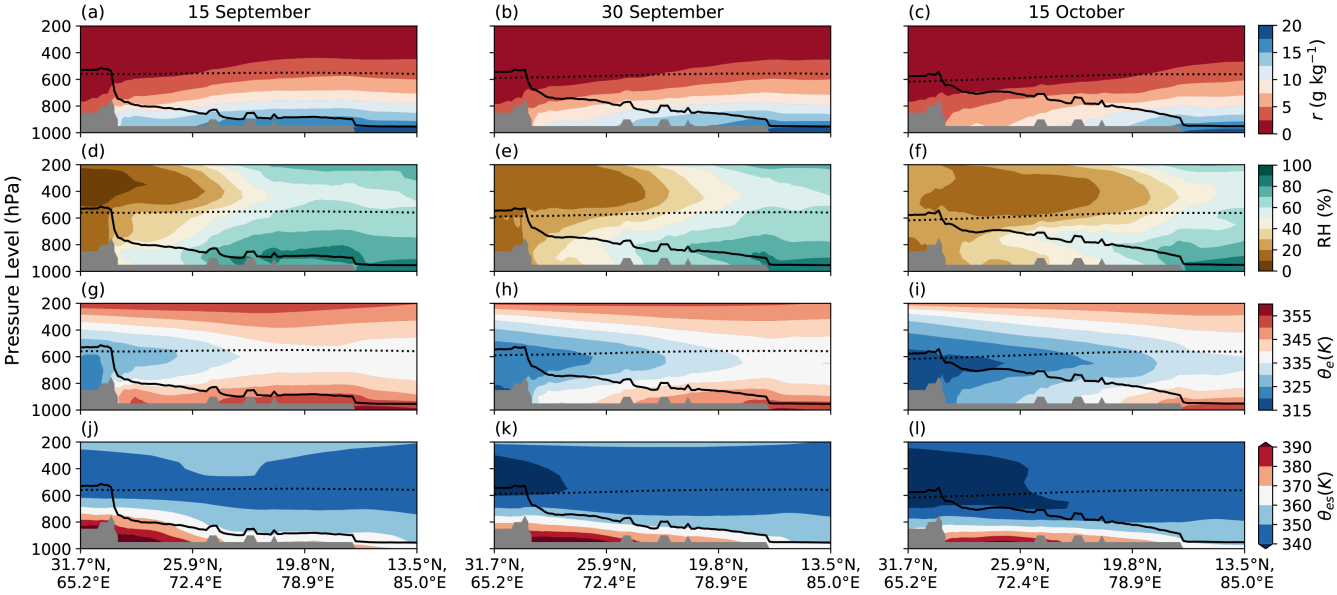

FIGURE 6 Northwest to southeast cross-sections of atmospheric thermodynamics on (a,d,g,j) September 15 (left), (b,e,h,k) September 30 (middle), and (c,f,i,l) October 15 (right) over the years 1940–2022. The panels show (a–c) water-vapour mixing ratio (g·kg^{-1}), (d–f) relative humidity (%), (g–i) equivalent potential temperature (K), and (j–l) saturation equivalent potential temperature (K). A solid black line in each subplot shows the lifting condensation level (LCL), whereas a dotted black line shows the freezing level. At each grid point along the transect, the LCL is identified with respect to the corresponding surface level. Grey areas show the orography. [Colour figure can be viewed at wileyonlinelibrary.com]

gradient in θ_{es} between the surface and 600 hPa over northwestern India, indicating a layer of low static stability. As the withdrawal progresses, this layer extends towards the southeast (Figure 6j–l). Since θ_{es} at a given pressure level is homomorphic with temperature (Parker *et al.*, 2016; Menon *et al.*, 2022), the warming at low levels over India during the withdrawal (Figure 5) is consistent with an increase in θ_{es}. This could be related to a combination of various processes, including, for example, a reduction in cloud cover (Figure 2) and a subsequent increase in the surface sensible heat flux; we will examine changes in surface fluxes in Section 6. In order to assess the quality of the ERA5 dataset during the back-extension period, we analyse vertical cross-sections of thermodynamic fields along the same transect for 1940–1958 and 1959–2022 (Figures S5 and S6). There are no noticeable differences between the two composites, suggesting the suitability of using the ERA5 dataset for the period 1940–2022.

The changes in θ_e and θ_{es} shown in Figure 6g–l can be related to changes in the environmental stability for deep convective clouds. Low static stability is associated with warming and cooling below and above 600 hPa, respectively. Given that the low-level θ_e is decreasing as the withdrawal progresses (Figure 6g–i), convective inhibition (CIN) tends to increase, whereas CAPE tends to decrease. Furthermore, the warming of low levels leads to an increasing tendency in CIN (Figure 6j–l), and the cooling of mid and high levels leads to an increasing tendency in CAPE. This suggests that CIN is being increased as the withdrawal progresses, but the contributions to CAPE from low and mid levels are opposing each other. Given that these changes in CAPE and CIN are accompanied by a general decrease in relative humidity at low levels, the likelihood of deep convection over India decreases with the progression of the withdrawal, which is consistent with the IRBT analysis in Figure 2. These results are reverse of those discussed by Parker *et al.* (2016) for the onset progression (see their section 4).

5.3 | Evolution of thermodynamic profiles over central India

We now examine closely the changes in thermodynamic fields at a grid point near Nagpur during the withdrawal. We choose Nagpur for this analysis, since it lies in central India and in the middle of the three locations considered in our previous analysis. Also, we can compare our results with those of Parker *et al.* (2016), who had also considered Nagpur for such an analysis.

Figure 7 shows the time series of vertical profiles of different thermodynamic fields over a two-month period centred on October 7, which is the climatological withdrawal date of the monsoon at Nagpur (Pai *et al.*, 2020). Nearly 30 days before the local monsoon withdrawal, there is a deep layer of high relative humidity, and the LCL is near

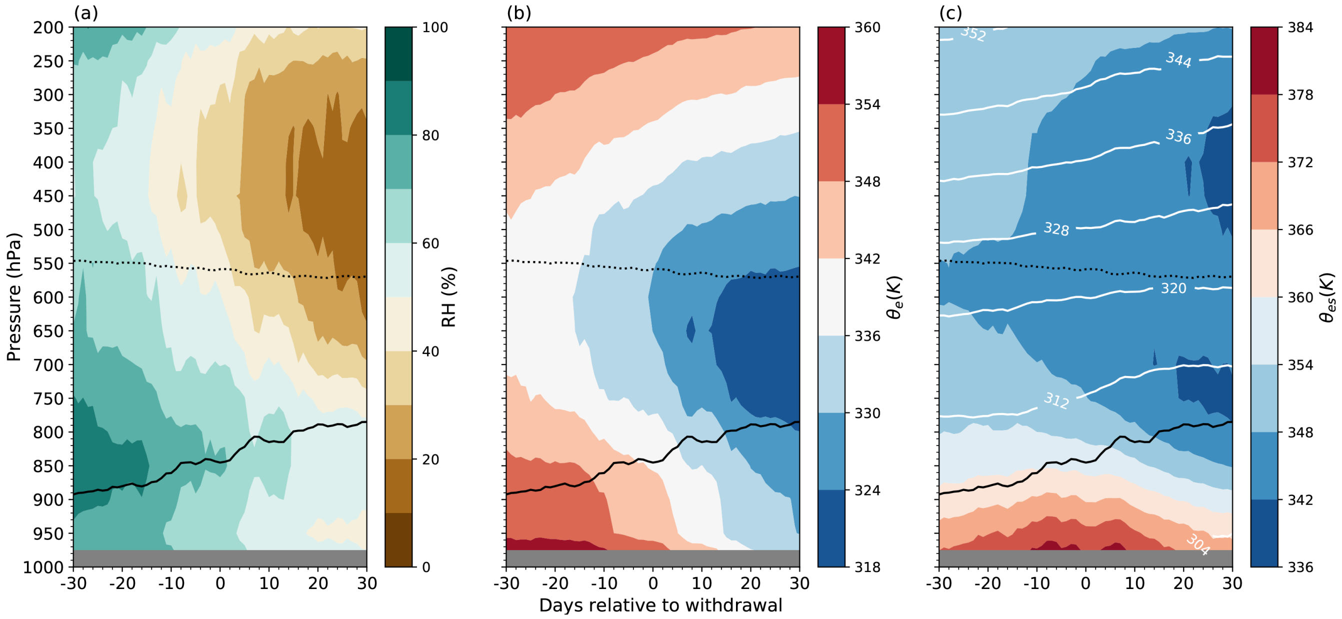

FIGURE 7 Time–pressure sections for Nagpur (21°N, 79°E) showing (a) relative humidity (%), (b) equivalent potential temperature (K), and (c) saturation equivalent potential temperature (K) during 1940–2022. All panels show the lifting condensation level (LCL; solid black) and freezing level (dotted black). In (c), white line contours show the virtual potential temperature (K). The profiles are computed for days relative to the climatological withdrawal of the monsoon from Nagpur (day 0 on the *x*-axis); the climatological withdrawal date is October 7 as per Pai et al. (2020). Grey areas show the orography. [Colour figure can be viewed at wileyonlinelibrary.com]

to 900 hPa (Figure 7a). These conditions are favourable for deep convection. Relative humidity is largest just above the LCL. Around 10 days before the withdrawal, a layer of dry air (relative humidity<50%) first appears at mid and upper levels (i.e., above 550 hPa). The relative humidity at low levels has already decreased by this time, and the LCL has risen to approximately 850 hPa. This confirms the results shown in Figures 3 and 6 that the dry intrusion is first initiated near mid levels even when low levels remain relatively moist. As the withdrawal date approaches, there is a further decrease in relative humidity at mid levels and low-θ_e air is advected into mid levels (Figure 7b). Subsequently, the height of the LCL and amount of dry air at various levels continue to increase, suppressing the development of deep convective clouds. These results are the reverse of those discussed by Parker *et al.* (2016) for the progression (see their section 4).

There is a strong vertical gradient in θ_{es} between the surface and 600 hPa nearly 30 days prior to the withdrawal (Figure 7c). The spacing between contours of virtual potential temperature at low levels can help determine whether the profile is dry adiabatic or pseudoadiabatic. For example, Parker *et al.* (2016) found a wide spacing between the 315 K and 320 K contours of virtual potential temperature over Nagpur in the pre-withdrawal period (see their fig. 8c), indicating a deep adiabatic layer below ~600 hPa. They found an abrupt decrease in the spacing between these contours as the monsoon progresses, indicating an abrupt transition from a dry adiabatic profile to a pseudoadiabatic profile. The spacing between the 312 K and 320 K contours of virtual potential temperature in the 800–600 hPa layer remains fairly uniform at all times (Figure 7c). This suggests that the transition of profiles during the withdrawal is not as abrupt compared with that seen during the onset progression.

In summary, an intrusion of mid-level low-θ_e air from the northwest increases the dry static stability, limiting the occurrence of deep convection towards the southeast coast of India. The evolution of vertical profiles of θ_e at Nagpur confirms the penetration of the mid-level low-θ_e air from around 10 days prior to the withdrawal. Compared with Jodhpur and Nagpur, the low-level profile at Vizag remains nearly pseudoadiabatic with a large CAPE at all times, which is associated with a relatively late withdrawal of the summer monsoon and onset of the winter monsoon. This favours the occurrence of deep convection.

6 | REGIMES IN SURFACE FLUXES

As discussed in Section 1, land–atmosphere interactions play a role in the progression of the monsoon. Here, we hypothesise that they could have a positive feedback on the withdrawal via changes in fluxes of heat and moisture from the surface. For example, as rains become less frequent in northwest India around the local withdrawal,

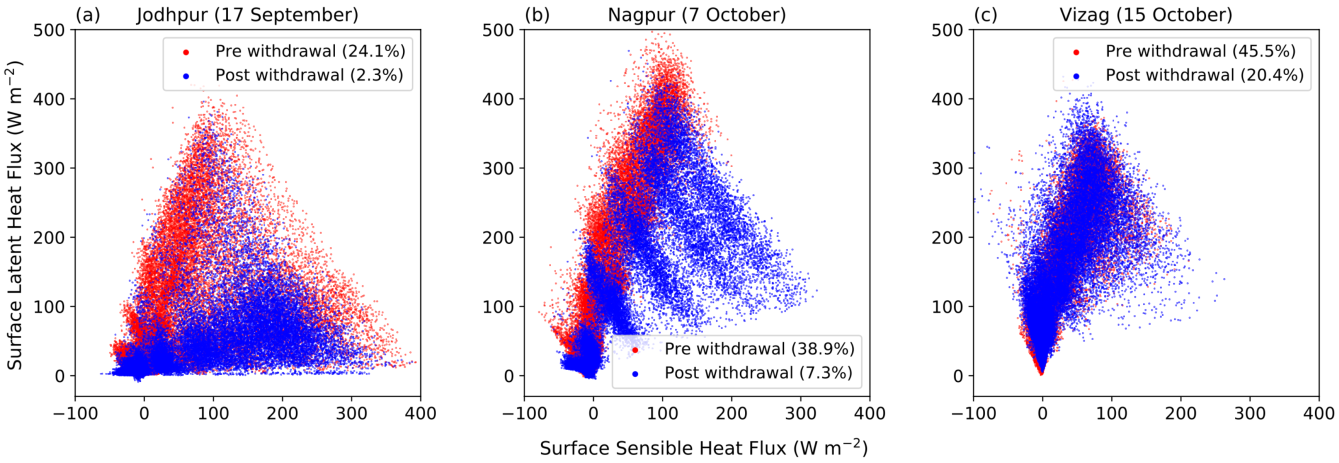

FIGURE 8 Scatter plots of hourly surface sensible heat flux ($\mathrm{W \cdot m^{-2}}$) and hourly surface latent heat flux ($\mathrm{W \cdot m^{-2}}$) at (a) Jodhpur, (b) Nagpur, and (c) Vizag during respective pre- and post-withdrawal phases of the monsoon. For each location, the pre-withdrawal phase refers to a period between 10 and 30 days (both inclusive) prior to the monsoon withdrawal, whereas the post-withdrawal phase refers to a period between 11 and 30 days (both inclusive) after the withdrawal. Fluxes are multiplied by minus one, due to which positive (negative) values show upward (downward) fluxes. The climatological withdrawal dates for each location as per the India Meteorological Department (IMD) are shown in the respective title. Figures in brackets in the legend show the frequency of rainfall occurrence (% of days). Surface fluxes are calculated using the ERA5 reanalysis data for the period 1940–2022, whereas the frequency of rainfall occurrence is determined using the APHRODITE dataset for the period 1951–2007. The IMD's standard rainy day threshold of 2.5 mm (i.e., daily rainfall≥2.5 mm) is used to define rainfall occurrence. [Colour figure can be viewed at wileyonlinelibrary.com]

the soil moisture is likely to deplete, causing a decrease in the evaporative fraction (ratio of latent heat flux to the sum of latent and sensible heat fluxes at the surface) and an increase in the boundary-layer height and CIN. This could make deep convection less likely on subsequent days. Turner *et al.* (2020) analysed data from flux towers at different sites in India during the 2016 INCOMPASS field campaign. They presented a comparison between surface fluxes at Jaisalmer (a semi-arid region near Jodhpur) and Samastipur (a region surrounded by rice cultivation fields in the Indo-Gangetic Plain) during August 2016. They observed two regimes in surface fluxes at Jaisalmer: whilst the overall surface energy budget in August 2016 was dominated by strong sensible heat flux, latent heat flux increased after rainfall. In contrast, surface fluxes at Samastipur featured a single regime that was dominated by strong latent heat flux. We use the ERA5 reanalysis dataset here to analyse hourly surface fluxes (i.e., at all hours) at grid points near Jodhpur, Nagpur, and Vizag during the pre- and post-withdrawal phases of the monsoon. Our analysis will determine whether such regimes exist and change during the pre- and post-withdrawal phases.

We first consider surface fluxes at the grid points closest to each station over a two-month period centred on the climatological withdrawal date. We then partition the data into terciles: the lower tercile comprises surface fluxes from 30 to 10 days inclusive before the withdrawal, whereas the upper tercile comprises surface fluxes over 11–30 days inclusive after the withdrawal. Figure 8 shows scatter plots of surface latent and sensible heat fluxes at the three sites. Values in brackets show the frequency of rainfall occurrence at each site, for which we follow previous studies (e.g., Turner *et al.*, 2020) that considered the IMD's standard rainy day threshold of≥2.5 mm. During the pre- and post-withdrawal periods, the surface sensible heat flux is strongest at Jodhpur (Figure 8a), whereas it is weakest at Vizag (Figure 8c). This shows the strong influence of solar heating at Jodhpur, where the frequency of rainfall occurrence is the smallest. Compared with Jodhpur and Nagpur, rainfall is more frequent at Vizag. Thus, a reduction in insolation due to cloud cover could be limiting the surface sensible heat flux. The surface latent heat flux is strongest at Nagpur (Figure 8b), where the soil is generally wetter than at other sites during the monsoon (e.g., Sravani *et al.*, 2022).

The scatter plots exhibit two regimes at Jodhpur and Nagpur. At Jodhpur, there are distinct regimes in which either latent or sensible heat fluxes dominate during the pre-withdrawal phase. However, there is a strong reduction in the latent heat flux during the post-withdrawal phase. This can be understood from the reduced frequency of rainfall occurrence from ∼24% to ∼2% between the pre- and post-withdrawal periods. At Nagpur, the pre-withdrawal phase is dominated by a stronger latent heat flux, which is replaced by stronger sensible heat flux during the post-withdrawal phase. Compared with Jodhpur, there is a larger decline in the frequency of rainfall occurrence at this location; the frequency

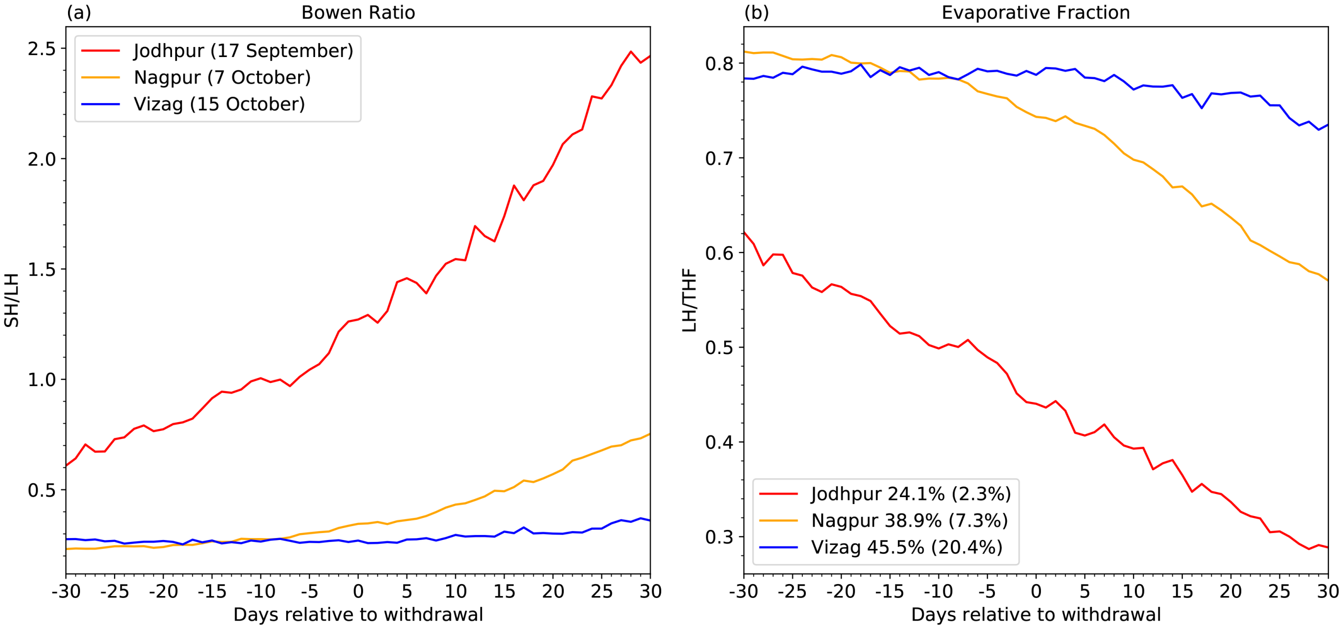

FIGURE 9 Time series of (a) Bowen ratio (ratio of surface sensible heat flux to surface latent heat flux) and (b) evaporative fraction (ratio of surface latent heat flux to the total surface flux) computed at grid points near Jodhpur, Nagpur, and Vizag. Surface fluxes are considered at 0700 UTC (12.30 pm Indian Standard Time) for days relative to the climatological withdrawal of the monsoon at each location (day 0 on the *x*-axis) over the period 1940–2022. The legend in (a) shows the climatological withdrawal date for each location. The legend in (b) shows the frequency of rainfall occurrence (% of days) between 10 and 30 days (both inclusive) prior to local withdrawal, whereas numbers in brackets show the frequency of rainfall occurrence between 11 and 30 days (both inclusive) after local withdrawal. [Colour figure can be viewed at wileyonlinelibrary.com]

decreases from ~40% to ~7% between the two periods. At Vizag, surface latent heat flux exceeds surface sensible heat flux in nearly all cases in the two phases. As discussed before, there is a greater influence of the monsoon at Vizag, which also witnesses the winter monsoon after the withdrawal of the southwest monsoon around mid-October. This could be inferred from a much larger frequency of rainfall occurrence during the pre-withdrawal (~46%) as well as post-withdrawal (~20%) periods than is observed at Jodhpur and Nagpur.

To understand better how the partitioning of surface fluxes changes during the withdrawal, we calculate the Bowen ratio (ratio of sensible to latent heat fluxes at the surface) and evaporative fraction at 0700 UTC (12:30 pm local time) when surface fluxes are largest (Figure 9). There is a consistent increase in the Bowen ratio (Figure 9a) and decrease in evaporative fraction (Figure 9b) at Jodhpur, with the sensible heat flux dominating after the local withdrawal. The increase in Bowen ratio and decrease in evaporative fraction at Nagpur are smaller than those at Jodhpur, whereas the Bowen ratio and evaporative fraction are nearly constant at Vizag at all times. Thus, land–atmosphere interactions likely have a positive feedback on the withdrawal process, which could be tested in model experiments in a future study.

In summary, the monsoon withdrawal leaves a strong footprint on surface fluxes at Jodhpur and Nagpur, where the surface energy budget is dominated by a stronger sensible heat flux during the post-withdrawal period when the frequency of rainfall occurrence is much reduced. This, however, is not true for Vizag, where there is no clear change in the distribution of surface latent heat flux and surface sensible heat flux between the two periods.

7 | CONCLUSIONS

The Indian summer monsoon (hereafter "the monsoon") is considered to be the lifeblood of India, since it supplies over 75% of the annual precipitation, providing water to over a billion people. The way in which the monsoon withdraws from the country determines the length of the rainy season at different locations, how much water is available for rain-fed agriculture, and whether summer crops become damaged during harvest. Despite this, the withdrawal has received less attention than the onset progression in the scientific literature. In this study, we used observations and the ERA5 reanalysis to understand the role of the midlatitudes in determining the direction of the withdrawal, for which we adapt the research framework of Parker *et al.* (2016) that was conceived for the onset. Our study is a key starting point for avenues of future research that elucidate the controls on pace and steadiness of the withdrawal. The summary of the key findings of our

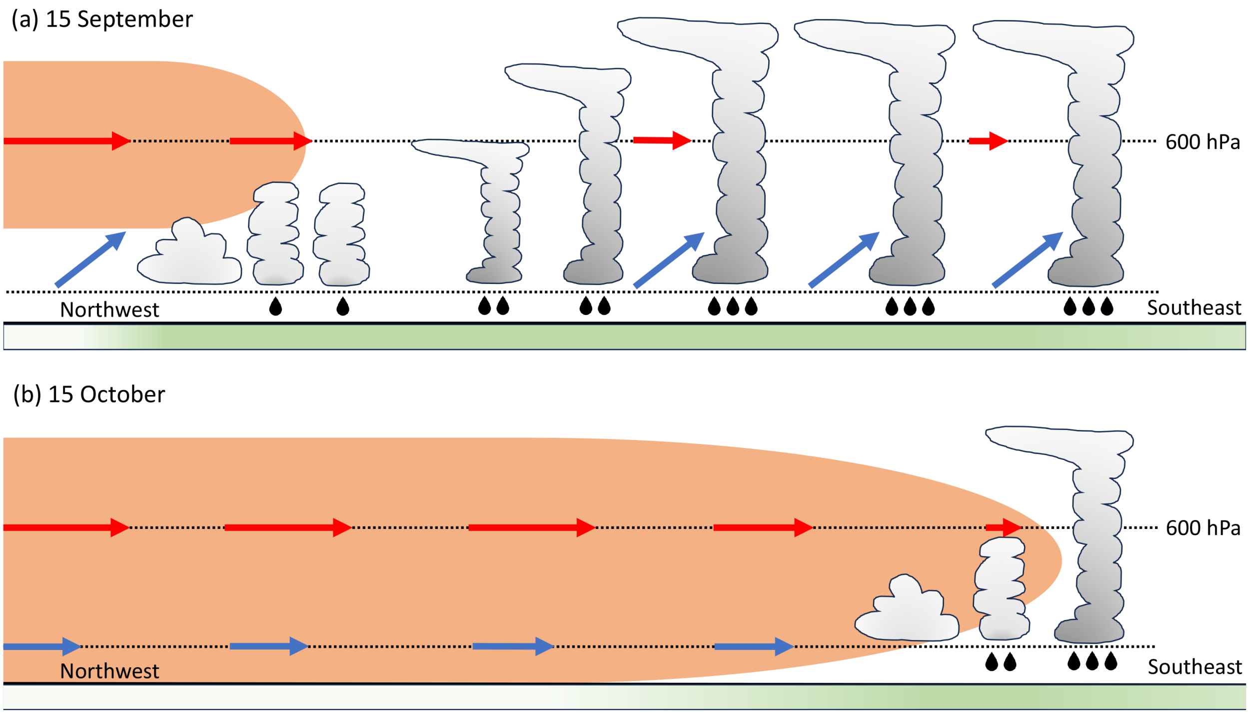

FIGURE 10 Schematic diagram encapsulating the role of dry air (brown shading) in the withdrawal of the Indian summer monsoon. The schematic diagram is drawn for a transect (shown in Figure 1) between northwestern India and the southeast coast. (a) shows the situation on September 15, which is around the climatological monsoon withdrawal date for northwestern India, and (b) shows the situation on October 15, which is the climatological withdrawal date for entire India. Red (blue) horizontal arrows show wind vectors at 600 hPa (near-surface level); the wind is westerly or southwesterly at low levels on September 15, northwesterly at low levels on October 15, and northwesterly at mid-levels on both dates. Typical clouds and intensity of precipitation on both dates are shown; the height of clouds is estimated using the ISCCP dataset. Green shading in both panels indicates the magnitude of the evaporative fraction (ratio of surface latent heat flux to total surface flux), with darker colours indicating a stronger evaporative flux toward the southeast coast on both dates. [Colour figure can be viewed at wileyonlinelibrary.com]

study, which is illustrated schematically in Figure 10, is as follows.

- Light precipitation is observed over northwestern India during early September, which is around two weeks prior to commencement of the withdrawal. Compared with this region, more frequent deep convection and more intense rainfall are observed over other parts of the country.
- Around mid-September, mid-tropospheric dry air is first observed over northwestern India. It suppresses deep convection there, and the monsoon begins to withdraw from this region.
- In subsequent days, the mid-level dry air strengthens and flows toward the southeast, stabilising the troposphere. Deep convection retreats and the withdrawal progresses toward the southeast.
- The monsoon withdraws from the entire northern India by September 30. Trajectories terminating at 600 hPa over this region arrive mostly from arid regions to the northwest of India, while those terminating at low levels also start arriving from the northwest.
- By October 15, the mid-level dry air engulfs most of India, leading to the withdrawal from the entire country. Almost all trajectories terminating at mid and low levels arrive from the northwest rather than oceanic sources and are predominantly descending in nature.

The results of our study suggest that the intrusion of mid-tropospheric dry air, which emanates from the midlatitudes, drives the southeastward progression of the withdrawal. Thus, the mechanism driving progression of the withdrawal can be considered as the reverse of that at play during progression of the onset (Parker *et al.*, 2016). The novelty of our work is that it establishes a firm relationship between the climatological intrusion of mid-level dry air and the southeastward progression of the withdrawal. Given that the subtropical jet stream shifts southward after mid-September, the dry intrusion could be associated with upper-level disturbances (e.g., troughs or blocking anticyclones) along the subtropical jet. Similar examples of mid-level dry intrusions originating from disturbances in the subtropical jet are observed in other regions such as the southern Maritime Continent (Aslam *et al.*, 2023).

Here, we analysed the climatological withdrawal, which is a necessary first step. It gives the impression that the withdrawal is a steady process. However, the withdrawal often exhibits hiatuses (e.g., the stalled withdrawal over central India for around two weeks during October 2020: India Meteorological Department, 2020). This suggests that the dry intrusion could be pulsing back and forth during the withdrawal phase; the mechanisms controlling such behaviour need to be explored in a future study, for which a combined Eulerian–Lagrangian analysis could be performed (e.g., as in the single-year case study of the onset by Volonté *et al.*, 2020). As discussed in Section 1, the withdrawal exhibits strong interannual variability, with previous studies attributing this to variations in the position of the South Asian High and subtropical jet (Agrawal & Pandey, 2022). Thus, researchers could explore the relationship between the position of the South Asian High, subtropical jet, and mid-tropospheric dry intrusions during the withdrawal in future studies. More detailed analysis is needed to fully explain and quantify the relative roles of midlatitude and tropical controls on the pace and steadiness of the withdrawal. Lastly, the representation of the interaction between the mid-level dry air and moist convection needs to be analysed in numerical weather prediction models in order to understand the potential to improve predictions of the withdrawal. This is important, since skilful predictions of the withdrawal at long lead times could benefit stakeholders (e.g., farmers) by giving them more time for planning. Researchers could use reforecast datasets, such as the Subseasonal-to-Seasonal prediction models (Vitart *et al.*, 2017) or hindcast simulations of coupled initialised seasonal prediction systems, for such studies.

ACKNOWLEDGEMENTS

A. Deoras, A. G. Turner, and A. Volonté were funded under the MiLCMOP project (NERC grant number NE/X000176/1). A. Menon is funded by the Met Office Weather and Climate Science for Service Partnership (WCSSP) India project, which is supported by the UK Department for Science, Innovation and Technology (DSIT). WCSSP India is a collaborative initiative between the Met Office and the Indian Ministry of Earth Sciences (MoES).

FUNDING INFORMATION

MiLCMOP project, funded by the Natural Environment Research Council, grant number: NE/X000176/1; Weather and Climate Science for Service Partnership (WCSSP) India project, a collaborative initiative between the Met Office, supported by the UK Department for Science, Innovation and Technology (DSIT), and the Indian Ministry of Earth Sciences (MoES).

DATA AVAILABILITY STATEMENT

The ERA5 hourly data on pressure levels are available at https://doi.org/10.24381/cds.bd0915c6. The APHRODITE gridded dataset is available at http://aphrodite.st.hirosaki-u.ac.jp/download/. The MERGIR and radiosonde datasets are available at https://disc.gsfc.nasa.gov/datasets/GPM_MERGIR_1/summary and https://www.ncei.noaa.gov/data/integrated-global-radiosonde-archive/access/data-por/, respectively. The ISCCP H-series dataset is available at https://www.ncei.noaa.gov/data/international-satellite-cloud-climate-project-isccp-h-series-data/access/isccp-basic/hgg/. The LAGRANTO Lagrangian analysis tool can be downloaded from http://iacweb.ethz.ch/staff/sprenger/lagranto/download.html. The Python interface for LAGRANTO, in which scripts for the trajectory calculations used in this article were created, is available at https://github.com/leosaffin/pylagranto. The climatological isochrones of the monsoon withdrawal were digitised from fig. 10b of Pai *et al.* (2020) using the WebPlotDigitizer software (https://automeris.io/WebPlotDigitizer). The Kernel density estimate maps of trajectory points displayed in Figure 4 are produced using https://seaborn.pydata.org/generated/seaborn.kdeplot.html.

ENDNOTES

[1] The climatological withdrawal date of the monsoon for northwestern India used to be September 1. The IMD revised climatological dates of the progression and withdrawal of the monsoon in 2020 (Pai *et al.*, 2020). The old dates were derived from the analysis of rainfall from 149 rain-gauge stations over the period 1901–1940. The number of rain-gauge stations has increased since then (e.g., Pai *et al.*, 2014), so the revised climatological dates are based on the analysis of rainfall during a recent climatological period (1961–2019 for onset and 1971–2019 for withdrawal).

[2] Note that the isochrone for September 15 is not shown, since the withdrawal initiates on September 17 (Pai *et al.*, 2020).

[3] Parker *et al.* (2016) have shown the evolution of precipitation from the pre-monsoon period to the monsoon (see their fig. 2). We follow this approach, although instead we are considering the evolution of precipitation and IRBT from the monsoon to the post-monsoon.

ORCID

Akshay Deoras https://orcid.org/0009-0006-5407-6520
Andrew G. Turner https://orcid.org/0000-0002-0642-6876
Ambrogio Volonté https://orcid.org/0000-0003-0278-952X
Arathy Menon https://orcid.org/0000-0001-9347-0578

REFERENCES

Agrawal, N. & Pandey, V.K. (2022) Evaluating the role of South Asian High on the transition phase of the Indian summer monsoon. *Theoretical and Applied Climatology*, 1511–1523. Available from: https://doi.org/10.1007/s00704-021-03890-9

Amale, H.S., Birthal, P.S. & Negi, D.S. (2023) Delayed monsoon, irrigation and crop yields. *Agricultural Economics*, 54, 77–94. Available from: https://doi.org/10.1111/agec.12746

Ananthakrishnan, R. & Soman, M. (1988) The onset of the southwest monsoon over Kerala: 1901–1980. *Journal of Climatology*, 8, 283–296. Available from: https://doi.org/10.1002/joc.3370080305

Arora, S.K., Bhan, S.C., Das, A.K., Durai, V.R., Goyal, S., Kaur, S. et al. (2014) *Monsoon 2013: A Report*. Tech. rep. Pune: India Meteorological Department. Available from: https://www.tropmet.res.in/~kolli/MOL/Monsoon/year2013/Monsoon-2013-NEW.pdf

Aslam, A.A., Schwendike, J., Peatman, S.C., Birch, C.E., Bollasina, M.A. & Barrett, P. (2023) Mid-Level Dry Air Intrusions over the southern Maritime Continent. *Quarterly Journal of the Royal Meteorological Society*, 150, 727–745. Available from: https://doi.org/10.1002/qj.4618

Asoka, A., Wada, Y., Fishman, R. & Mishra, V. (2018) Strong linkage between precipitation intensity and monsoon season groundwater recharge in India. *Geophysical Research Letters*, 45, 5536–5544. Available from: https://doi.org/10.1029/2018GL078466

Betts, A.K. (1986) A new convective adjustment scheme. Part I: Observational and theoretical basis. *Quarterly Journal of the Royal Meteorological Society*, 112, 677–691. Available from: https://doi.org/10.1002/qj.49711247307

Bhat, G.S. (2006) The Indian drought of 2002—a sub-seasonal phenomenon? *Quarterly Journal of the Royal Meteorological Society*, 132, 2583–2602. Available from: https://doi.org/10.1256/qj.05.13

Bollasina, M.A. & Ming, Y. (2013) The role of land-surface processes in modulating the Indian monsoon annual cycle. *Climate Dynamics*, 41, 2497–2509. Available from: https://doi.org/10.1007/s00382-012-1634-3

Boos, W.R. & Kuang, Z. (2010) Dominant control of the South Asian monsoon by orographic insulation versus plateau heating. *Nature*, 463, 218–222. Available from: https://doi.org/10.1038/nature08707

Flohn, H. (1957) Large-scale aspects of the “summer monsoon” in South and East Asia. *Journal of the Meteorological Society of Japan. Ser. II*, 35, 180–186.

Gadgil, S. & Gadgil, S. (2006) The Indian monsoon, GDP and agriculture. *Economic and Political Weekly*, 41, 4887–4895.

Hersbach, H. (2023) *ERA5 Reanalysis Now Available From 1940*. Reading: ECMWF Newsletter. Available from: https://www.ecmwf.int/en/newsletter/175/news/era5-reanalysis-now-available-1940

Hersbach, H., Bell, B., Berrisford, P., Hirahara, S., Horányi, A., Muñoz-Sabater, J. et al. (2020) The ERA5 global reanalysis. *Quarterly Journal of the Royal Meteorological Society*, 146, 1999–2049. Available from: https://doi.org/10.1002/qj.3803

India Meteorological Department. (2020) Southwest Monsoon End of Season Report. https://internal.imd.gov.in/press_release/20201220_pr_963.pdf

Janowiak, J.E., Joyce, R.J. & Yarosh, Y. (2001) A real-time global half-hourly pixel-resolution infrared dataset and its applications. *Bulletin of the American Meteorological Society*, 82, 205–218. Available from: https://doi.org/10.1175/1520-0477(2001)082<0205:ARTGHH>2.3.CO;2

Koteswaram, P. (1958) The easterly jet stream in the tropics. *Tellus*, 10, 43–57. Available from: https://doi.org/10.3402/tellusa.v10i1.9220

Krishnamurti, T., Simon, A., Thomas, A., Mishra, A., Sikka, D., Niyogi, D. et al. (2012) Modeling of forecast sensitivity on the march of monsoon isochrones from Kerala to New Delhi: the first 25 days. *Journal of the Atmospheric Sciences*, 69, 2465–2487. Available from: https://doi.org/10.1175/JAS-D-11-0170.1

Krishnamurti, T., Thomas, A., Simon, A. & Kumar, V. (2010) Desert air incursions, an overlooked aspect, for the dry spells of the Indian summer monsoon. *Journal of the Atmospheric Sciences*, 67, 3423–3441. Available from: https://doi.org/10.1175/2010JAS3440.1

Madonna, E., Wernli, H., Joos, H. & Martius, O. (2014) Warm conveyor belts in the ERA-Interim dataset (1979–2010). Part I: Climatology and potential vorticity evolution. *Journal of Climate*, 27, 3–26. Available from: https://doi.org/10.1175/JCLI-D-12-00720.1

Martens, B., Schumacher, D.L., Wouters, H., Muñoz-Sabater, J., Verhoest, N.E. & Miralles, D.G. (2020) Evaluating the land-surface energy partitioning in ERA5. *Geoscientific Model Development*, 13, 4159–4181. Available from: https://doi.org/10.5194/gmd-13-4159-2020

Menon, A., Turner, A.G., Volonté, A., Taylor, C.M., Webster, S. & Martin, G. (2022) The role of mid-tropospheric moistening and land-surface wetting in the progression of the 2016 Indian monsoon. *Quarterly Journal of the Royal Meteorological Society*, 148, 3033–3055. Available from: https://doi.org/10.1002/qj.4183

Mohanty, U., Pearce, R.P. & Tiedtke, M. (1984) *Numerical Experiments on the Simulation of the 1979 Asian Summer Monsoon*, Vol. 44. Reading: European Centre for Medium Range Weather Forecasts.

Noska, R. & Misra, V. (2016) Characterizing the onset and demise of the Indian summer monsoon. *Geophysical Research Letters*, 43, 4547–4554. Available from: https://doi.org/10.1002/2016GL068409

Pai, D., Arti, B., Sunitha, D., Madhuri, M., Badwaik, M., Kundale, A. et al. (2020) Normal dates of onset/progress and withdrawal of southwest monsoon over India. *Mausam*, 71, 553–570. Available from: https://doi.org/10.54302/mausam.v71i4.33

Pai, D., Rajeevan, M., Sreejith, O., Mukhopadhyay, B. & Satbha, N. (2014) Development of a new high spatial resolution (0.25× 0.25) long period (1901-2010) daily gridded rainfall data set over India and its comparison with existing data sets over the region. *Mausam*, 65, 1–18.

Parker, D.J., Willetts, P., Birch, C., Turner, A.G., Marsham, J.H., Taylor, C.M. et al. (2016) The interaction of moist convection and mid-level dry air in the advance of the onset of the Indian monsoon. *Quarterly Journal of the Royal Meteorological Society*, 142, 2256–2272. Available from: https://doi.org/10.1002/qj.2815

Parthasarathy, B. & Mooley, D. (1978) Some features of a long homogeneous series of Indian summer monsoon rainfall. *Monthly Weather Review*, 106, 771–781. Available from: https://doi.org/10.1175/1520-0493(1978)106<0771:SFOALH>2.0.CO;2

Prakash, S., Mitra, A.K., Momin, I.M., Rajagopal, E., Basu, S., Collins, M. et al. (2015) Seasonal intercomparison of observational rainfall datasets over India during the southwest monsoon season. *International Journal of Climatology*, 35, 2326–2338. Available from: https://doi.org/10.1002/joc.4129

Prasanna, V. (2014) Impact of monsoon rainfall on the total foodgrain yield over India. *Journal of Earth System Science*, 123, 1129–1145. Available from: https://doi.org/10.1007/s12040-014-0444-x

Preethi, B. & Revadekar, J. (2013) Kharif foodgrain yield and daily summer monsoon precipitation over India. *International Journal *of Climatology*, 33, 1978–1986. Available from: https://doi.org/10.1002/joc.3565

Rai, D. & Raveh-Rubin, S. (2023) Enhancement of Indian summer monsoon rainfall by cross-equatorial dry intrusions. *Npj Climate and Atmospheric Science*, 6. Available from: https://doi.org/10.1038/s41612-023-00374-7

Raju, P., Mohanty, U. & Bhatla, R. (2005) Onset characteristics of the southwest monsoon over India. *International Journal of Climatology*, 25, 167–182. Available from: https://doi.org/10.1002/joc.1121

Rao, Y. (1976) Southwest monsoon, meteorological monograph synoptic meteorology, No. 1/1976. *India Meteorological Department*, 366.

Rossow, W.B., Knapp, K.R. & Young, A.H. (2022) International satellite cloud climatology project: Extending the record. *Journal of Climate*, 35, 141–158. Available from: https://doi.org/10.1175/JCLI-D-21-0157.1

Saha, K., Mooley, D. & Saha, S. (1979) The Indian monsoon and its economic impact. *GeoJournal*, 3, 171–178. Available from: https://doi.org/10.1007/BF00257706

Sankar, S., Achanya Unni, V., Abhilash, S., Abhiram Nirmal, C., Vijaykumar, P., Mohanakumar, K. et al. (2023) Contrasting features of northeast monsoon during 2019 and 2020 in response to the delayed withdrawal of southwest monsoon. *Theoretical and Applied Climatology*, 153, 19–34. Available from: https://doi.org/10.1007/s00704-023-04467-4

Singh, R. & Sandeep, S. (2022) Dynamics of dry air intrusion over India during summer monsoon breaks. *Climate Dynamics*, 59, 1649–1664. Available from: https://doi.org/10.1007/s00382-021-06060-9

Soman, M. & Kumar, K.K. (1993) Space-time evolution of meteorological features associated with the onset of Indian summer monsoon. *Monthly Weather Review*, 121, 1177–1194. Available from: https://doi.org/10.1175/1520-0493(1993)121%3C1177:STEOMF%3E2.0.CO;2

Sprenger, M. & Wernli, H. (2015) The LAGRANTO Lagrangian analysis tool–version 2.0. *Geoscientific Model Development*, 8, 2569–2586. Available from: https://doi.org/10.5194/gmd-8-2569-2015

Sravani, C., Kishore, P., Jiang, J.H. & Rao, S.V.B. (2022) Climatological changes in soil moisture during the 21st Century over the Indian Region Using CMIP5 and Satellite Observations. *Remote Sensing*, 14, 2108. Available from: https://doi.org/10.3390/rs14092108

Taylor, C.M., Belušić, D., Guichard, F., Parker, D.J., Vischel, T., Bock, O. et al. (2017) Frequency of extreme Sahelian storms tripled since 1982 in satellite observations. *Nature*, 544, 475–478. Available from: https://doi.org/10.1038/nature22069

Turner, A.G., Bhat, G., Martin, G., Parker, D.J., Taylor, C., Mitra, A.K. et al. (2020) Interaction of convective organization with monsoon precipitation, atmosphere, surface and sea: The 2016 INCOMPASS field campaign in India. *Quarterly Journal of the Royal Meteorological Society*, 146, 2828–2852. Available from: https://doi.org/10.1002/qj.3633

Vitart, F., Ardilouze, C., Bonet, A., Brookshaw, A., Chen, M., Codorean, C. et al. (2017) The subseasonal to seasonal (S2S) prediction project database. *Bulletin of the American Meteorological Society*, 98, 163–173. Available from: https://doi.org/10.1175/BAMS-D-16-0017.1

Volonté, A., Turner, A.G. & Menon, A. (2020) Airmass analysis of the processes driving the progression of the Indian summer monsoon. *Quarterly Journal of the Royal Meteorological Society*, 146, 2949–2980. Available from: https://doi.org/10.1002/qj.3700

Volonté, A., Turner, A.G., Schiemann, R., Luigi, V.P. & Klingaman, N.P. (2022) Characterising the interaction of tropical and extratropical air masses controlling East Asian summer monsoon progression using a novel frontal detection approach. *Weather and Climate Dynamics*, 3, 575–599. Available from: https://doi.org/10.5194/wcd-3-575-2022

Walker, J.M. & Bordoni, S. (2016) Onset and withdrawal of the large-scale South Asian monsoon: A dynamical definition using change point detection. *Geophysical Research Letters*, 43, 11–815. Available from: https://doi.org/10.1002/2016GL071026

Xavier, P.K., Marzin, C. & Goswami, B.N. (2007) An objective definition of the Indian summer monsoon season and a new perspective on the ENSO–monsoon relationship. *Quarterly Journal of the Royal Meteorological Society*, 133, 749–764. Available from: https://doi.org/10.1002/qj.45

Yanai, M., Li, C. & Song, Z. (1992) Seasonal heating of the Tibetan Plateau and its effects on the evolution of the Asian summer monsoon. *Journal of the Meteorological Society of Japan. Ser. II*, 70, 319–351. Available from: https://doi.org/10.2151/jmsj1965.70.1B.319

Yatagai, A., Kamiguchi, K., Arakawa, O., Hamada, A., Yasutomi, N. & Kitoh, A. (2012) APHRODITE: Constructing a long-term daily gridded precipitation dataset for Asia based on a dense network of rain gauges. *Bulletin of the American Meteorological Society*, 93, 1401–1415. Available from: https://doi.org/10.1175/BAMS-D-11-00122.1

Young, A.H., Knapp, K.R., Inamdar, A., Hankins, W. & Rossow, W.B. (2018) The international satellite cloud climatology project H-Series climate data record product. *Earth System Science Data*, 10, 583–593. Available from: https://doi.org/10.5194/essd-10-583-2018

Zaveri, E., Grogan, D.S., Fisher-Vanden, K., Frolking, S., Lammers, R.B., Wrenn, D.H. et al. (2016) Invisible water, visible impact: groundwater use and Indian agriculture under climate change. *Environmental Research Letters*, 11, 084005. Available from: https://doi.org/10.1088/1748-9326/11/8/084005

SUPPORTING INFORMATION

Additional supporting information can be found online in the Supporting Information section at the end of this article.

How to cite this article: Deoras, A., Turner, A.G., Volonté, A. & Menon, A. (2024) The role of midlatitude dry air during the withdrawal of the Indian summer monsoon. *Quarterly Journal of the Royal Meteorological Society*, 1–19. Available from: https://doi.org/10.1002/qj.4859